https://doi.org/10.5194/egusphere-2026-6582
Preprint. Discussion started: 9 November 2026
© Author(s) 2026. CC BY 4.0 License.

Orbital-scale climate forcing of atmospheric dust flux in the Middle Jurassic

Dawei Lv[a], Xinyi Ding[a], Zhihui Zhang[a,*], Guibo Zheng[a], Mehrdad Sardar Abadi[b], Jian Zhang[c], Zicheng Yu[d], Chengshan Wang[e], Munira Raji[f], Bing Wang[a]

[a] College of Earth Sciences and Engineering, Shandong University of Science and Technology, Qingdao 266590, China
[b] LIAG Institute for Applied Geophysics, Stilleweg 2, 30655 Hannover, Germany
[c] State Key Laboratory of Tibetan Plateau Earth System, Resources and Environment (TPESRE), Institute of Tibetan Plateau Research, Chinese Academy of Sciences, Beijing 100101, China
[d] School of Geographical Sciences, Northeast Normal University, Changchun 130024, China
[e] School of Earth Sciences and Resources, China University of Geosciences (Beijing), Beijing 100083, China
[f] Sustainable Earth Institute (SEI), University of Plymouth, Plymouth PL4 8AA, UK

Correspondence to: Zhihui Zhang (zhzhihui@sdust.edu.cn)

Abstract

Atmospheric dust fluxes are influenced by both human activities and natural climate variability, making it difficult to isolate climate-driven dust changes under modern warming. The Middle Jurassic greenhouse world provides a natural "experiment" to examine orbital-scale dust dynamics. Here, we reconstructed two high-resolution dust deposition records from mid- to high-latitude Middle Jurassic peatlands in China, using integrated petrographic, geochemical, palynological, isotopic, geochronological, and climate-model analyses. Our records reveal that the Junggar and Ordos basins hosted Aalenian ombrotrophic peatlands, with mineral matter primarily derived from atmospheric fallout, yielding atmospheric dust fluxes of 0.76–6.73 g m^{-2} a^{-1} and 1.53–27.36 g m^{-2} a^{-1}, respectively. Dust fluxes are significantly linked to the hydrological cycle paced by astronomical forcing: Within published astrochronologic frameworks, humid intervals and reduced dust accumulation covary at timescales corresponding to ~405 kyr eccentricity and ~20 kyr precession. We conclude that Middle Jurassic atmospheric dust flux was primarily controlled by orbitally driven precipitation changes.

Keywords: Atmospheric dust flux; Middle Jurassic; Orbital forcing; Ombrotrophic peatlands; Paleoclimate; Cyclostratigraphy

1 Introduction

Atmospheric dust is a critical component of the global Earth system, modulating radiative balance, cloud formation, and marine primary productivity (Jickells et al., 2005; Shao et al., 2011; Tagliabue et al., 2017). While modern dust cycles are increasingly influenced by anthropogenic activities, the Middle Jurassic greenhouse world offers a pristine "natural laboratory" to investigate how dust flux responds to orbital forcing under extreme warmth. Understanding these ancient dynamics is crucial, as they may provide insights into dust-climate interaction under future warming conditions with reduced polar ice volume.

https://doi.org/10.5194/egusphere-2026-6582
Preprint. Discussion started: 9 November 2026
© Author(s) 2026. CC BY 4.0 License.

Holocene studies demonstrate that, among various geological archives, ombrotrophic peatlands are considered efficient sinks for atmospheric deposition because their moisture supply depends entirely on precipitation (Shotyk, 1996; Le Roux et al., 2012; Wang et al., 2023). Therefore, despite the complex sources of mineral matter in coals throughout geological history (including biogenic, surface water, and authigenic origins; Andrejko et al., 1983a, 1983b; Bailey and Kosters, 1983; Davis et al., 1984; Shotyk, 1988; Triplehorn, 1990; Ruppert et al., 1991; Ward, 2016), ombrotrophic peatlands may preserve valuable records for reconstructing atmospheric dust fluxes. This understanding derived from modern processes provides a theoretical basis for extending dust records from the Quaternary into deep-time geological periods.

Although Quaternary records indicate that global dust flux responds significantly to orbital forcing (Cao et al., 2021), current understanding is largely established in the context of glacial–interglacial climatic oscillations (Sardar Abadi et al., 2021; Zhong et al., 2024). In contrast, the mechanisms through which orbital forcing influenced dust flux under greenhouse-climate conditions lacking ice-volume effects remain poorly constrained. In particular, high-resolution records that directly test whether dust deposition in mid- to high-latitude terrestrial settings during the Middle Jurassic was significantly influenced by orbitally paced hydroclimatic fluctuations are still lacking.

Accordingly, this study reconstructs two high-resolution Middle Jurassic dust deposition records from the Junggar and Ordos basins in China, using multiple proxies including coal macerals, ash content, palynology, and organic carbon isotopes ($\delta^{13}C_{org}$). This research aims to elucidate how orbital cycles (eccentricity and precession) modulated regional hydroclimate and atmospheric dust dynamics during the Middle Jurassic. Through comparison with other dust records, this study provides a deep-time perspective on how orbital forcing modulates atmospheric dust flux under greenhouse climate conditions.

2 Materials and methods

2.1 Geological background

During the Middle Jurassic, the Junggar and Ordos basins were located at mid- to high paleolatitudes in the Northern Hemisphere, with the Junggar Basin farther north than the Ordos Basin (Fig. 1a; Kent and Irving, 2010; Fang et al., 2019; Zhang et al., 2023; Olsen et al., 2024). In this paleogeographic setting, the basins may have been influenced by prevailing mid-latitude westerly circulation, which could have facilitated long-distance aeolian dust transport across northern Asia (Jiang et al., 2001; Zhong et al., 2024). Although exact dust sources remain unconstrained, surrounding highlands may have modified wind pathways, while exposed alluvial plains, seasonally dry basin margins, and weathered uplands may have served as potential dust-producing areas.

https://doi.org/10.5194/egusphere-2026-6582
Preprint. Discussion started: 9 November 2026
© Author(s) 2026. CC BY 4.0 License.

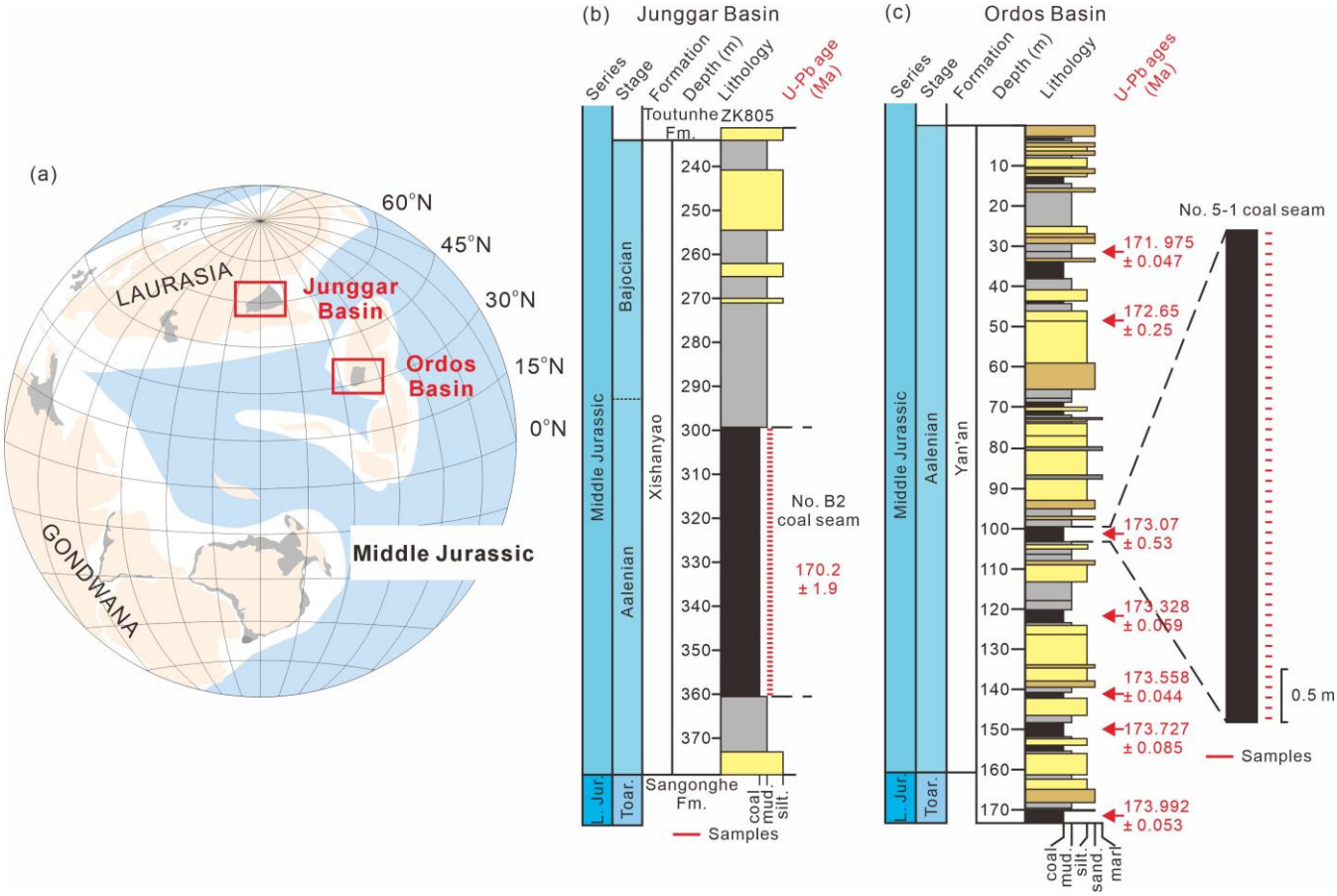


Figure 1. Location and stratigraphy. (a) Paleogeographic positions of the Junggar and Ordos basins (modified from Scotese, 2016). (b) Stratigraphic column of the Middle Jurassic Xishanyao Formation in the Junggar Basin (after Lv et al., 2025). (c) Stratigraphic column of the Middle Jurassic Yan'an Formation in the Ordos Basin (after Zhang et al., 2021).

The Aalenian Xishanyao and Yan'an formations are fluvial–lacustrine to lacustrine-deltaic coal-bearing successions, but previous sedimentological studies indicate that the sampled coal seams formed in mire or swamp settings rather than active channel-fill deposits or intervals directly dominated by riverine clastic supply (Johnson et al., 1989; Bian et al., 2010; Li et al., 2014; Lv et al., 2023). This is supported by the lack of channel-related clastic layers and by geochemical separation from coeval fluvial clastic rocks.

We collected 58 and 48 samples from the ~60 m No. B2 coal seam in the Zhundong Coalfield, Junggar Basin, and the ~5 m No. 5-1 coal seam in the Dongsheng Coalfield, Ordos Basin, at 1.05 m and 10 cm intervals, respectively (Figs. 1b, c).

https://doi.org/10.5194/egusphere-2026-6582
Preprint. Discussion started: 9 November 2026
© Author(s) 2026. CC BY 4.0 License.

2.2 Sample analyses and analytical approach

2.2.1 Coal petrography and coal-facies indices

Coal maceral analysis was conducted at Shandong University of Science and Technology following the standards of the International Committee for Coal and Organic Petrology (ICCP, 2001). At least 500 points were counted for each sample. To reconstruct peat-forming environments, the groundwater influence index (GWI) and vegetation index (VI) were calculated following Calder et al. (1991):

$$GWI=\frac{gelocollinite+corpocollinite+mineral\ matter}{telinite+telocollinite+desmocollinite} \quad (1)$$

$$VI=\frac{telinite+telocollinite+fusinite+semifusinite+suberinite+resinite}{desmocollinite+inertodetrinite+alginite+liptodetrinite+sporinite+cutinite} \quad (2)$$

GWI reflects the degree of groundwater influence during peat accumulation, whereas VI reflects the relative contribution of woody versus herbaceous vegetation to the peat-forming mire. Ombrotrophic conditions were identified using a GWI threshold of < 1.0 together with ash yield < 10 %. These criteria were used to identify ombrotrophic mire conditions and to evaluate the potential influence of groundwater or surface-water input.

2.2.2 Coal chemistry and stable carbon isotopes

Proximate analysis, total organic carbon (TOC), and bulk organic carbon isotopic composition ($\delta^{13}C_{org}$) were analyzed at Shandong University of Science and Technology. Ash yield and apparent density (ARD) were determined according to ASTM D3174-12(2018) and GB/T 6949-2010, respectively. During analysis, weighing precision was maintained at 0.0001 g, with repeatability limits of 0.10 % for ash yield and 0.04 g cm^{-3} for ARD. TOC was measured using a LECO CS-230 carbon-sulfur analyzer following GB/T 19145-2003. The $\delta^{13}C_{org}$ values were determined using a MAT-253 isotope ratio mass spectrometer coupled to a Micro Cube elemental analyzer and are reported relative to Vienna Pee Dee Belemnite (VPDB). The analytical uncertainty for $\delta^{13}C_{org}$ was ±0.1 ‰.

2.2.3 Major- and trace-element geochemistry and provenance comparison

Major- and trace-element analyses of the Xishanyao Formation coal samples were conducted at Shandong University of Science and Technology. Samples were ground to <200 mesh and oven-dried at 105–110 °C for 2 h to remove moisture. For major-element analysis, approximately 1 g of powdered sample was placed in a platinum crucible and heated in a muffle furnace to 650 °C over 1 h, followed by ignition at this temperature for 0.5–1 h to remove organic matter and determine loss on ignition. Major-element oxides in the resulting ash were measured by X-ray fluorescence spectrometry (XRF; PW2404), and the results were converted to concentrations on a whole-coal basis.

Trace elements were determined by inductively coupled plasma-mass spectrometry (ICP-MS). Approximately 50 ± 1 mg of powdered sample was digested with 2 mL HNO_3 and 1.5 mL HF in a sealed vessel at 190 °C for 48 h. After addition of 1 mL

https://doi.org/10.5194/egusphere-2026-6582
Preprint. Discussion started: 9 November 2026
© Author(s) 2026. CC BY 4.0 License.

concentrated HNO_3 and 1 mL ultrapure water, the samples were heated again at 190 °C for 24 h. The final solutions were diluted to 100 mL with 2 % HNO_3 prior to ICP-MS analysis.

To evaluate the provenance characteristics of mineral matter preserved in the coal seams, the Xishanyao coal geochemical data were compared with published coeval clastic-rock data from Wang et al. (2024). For the Yan'an Formation, major- and trace-element data for 16 samples from the No. 5-1 coal seam were compiled from L. Wang et al. (2022), whereas major-element data for regional green sandstones were obtained from Bai et al. (2025) and trace- and rare-earth-element data for sandstones were obtained from Y. Li et al. (2022). Source-rock affinities were evaluated using Al_2O_3-TiO_2 discrimination diagrams following Hayashi et al. (1997), with emphasis on the proportions of samples plotting within mafic-, intermediate-, and felsic-source fields rather than on their absolute positions in Al_2O_3-TiO_2 space. La/Sc and Co/Th ratios were additionally used as relatively immobile trace-element provenance indicators. These geochemical comparisons were used to assess differences in provenance distributions between coal-hosted mineral matter and regional clastic sediments, rather than as an independent criterion for distinguishing aeolian from fluvial transport.

2.2.4 Detrital zircon U–Pb dating

Detrital zircon U–Pb dating was conducted at Shandong University of Science and Technology using conventional mineral-separation procedures. After crushing, grinding, sieving, heavy-liquid separation, and magnetic separation, separated zircon grains were mounted and examined by cathodoluminescence imaging prior to U–Pb analysis. Analytical spots were selected on suitable domains while avoiding visible cracks and inclusions where possible. U–Pb isotope analyses were performed using laser ablation–inductively coupled plasma–mass spectrometry (LA-ICP-MS) on an Agilent 7900 platform, following the analytical procedures of Liu et al. (2008, 2010). For the coal-hosted zircon datasets, the concordance values reported by the analytical laboratories were retained, and sample analyses with reported concordance <90 % were excluded from provenance and age-distribution comparisons. This screening retained 62 of 76 sample analyses for the No. B2 coal seam and 70 of 80 sample analyses for the No. 5-1 coal seam. Preferred ages were assigned after concordance screening: $^{206}Pb/^{238}U$ ages were used for grains younger than 1000 Ma, whereas $^{207}Pb/^{206}Pb$ ages were used for grains older than 1000 Ma.

2.2.5 Palynology and detrended correspondence analysis

Palynological samples were processed at the palynology laboratory of the Institute of Geology, Chinese Academy of Geological Sciences, following the standard palynological preparation procedure SY/T 5915-2000. To prepare the abundance data for multivariate analysis, the selected spore-pollen taxa were standardized using the Wisconsin double-standardization method, which first divides each taxon by its maximum abundance and then normalizes by sample totals. The standardized abundance matrix was subsequently analyzed using detrended correspondence analysis (DCA) in PAST 4.09 to extract the major gradients in palynological composition (Hammer et al., 2001). Because DCA axes represent compositional gradients rather than climatic variables per se, their environmental significance was interpreted by comparing the ordination positions and stratigraphic distributions of taxa with the ecological affinities and climate preferences of their parent plants. On this basis,

https://doi.org/10.5194/egusphere-2026-6582
Preprint. Discussion started: 9 November 2026
© Author(s) 2026. CC BY 4.0 License.

the horizontal gradient was interpreted as a humidity-related compositional gradient and the vertical gradient as a temperature-related compositional gradient. Higher scores along the humidity-related axis were interpreted to represent relatively drier conditions, whereas higher scores along the temperature-related axis were interpreted to represent relatively cooler conditions.

2.2.6 Dust deposition rate calculation

The atmospheric dust deposition rate (DDR) in the paleo-peatlands was calculated using a mass accumulation approach:

$$\mathrm{DDR} = A_{\mathrm{ad}} \times \rho \times S \times 10 \quad (3)$$

where A_{ad} is the air-dried-basis ash yield expressed in wt.%, ρ is the apparent density of coal (g cm^{-3}), and S is the linear sedimentation rate (m kyr^{-1}). The factor of 10 accounts for the percentage conversion of ash yield, the conversion from g cm^{-3} to g m^{-3} and from kyr to yr, yielding DDR in g m^{-2} a^{-1}.

The use of coal ash as a first-order indicator of atmospheric mineral input follows the rationale of Marshall et al. (2016), who demonstrated that a substantial proportion of inorganic matter in coal may be supplied by atmospheric dust. Unlike the carbon-accumulation-based method of Marshall et al. (2016), the present study calculates DDR directly using measured ash yield and apparent density together with linear sedimentation rates.

This approach assumes that ash content predominantly reflects atmospheric mineral input and that post-depositional alteration does not substantially modify relative dust trends. The sedimentation rates used for DDR calculation were adopted from the astronomically constrained estimates of Zhang et al. (2020) and Lv et al. (2025). Because S derives from astronomically tuned age models and peat accumulation may have varied through time, DDR is used mainly to evaluate relative dust trends and phase relationships with humidity, rather than to overinterpret absolute flux magnitudes or treat DDR periodicities as fully independent evidence for orbital forcing.

2.2.7 Cyclostratigraphic analysis

Prior to spectral analysis, the relative temperature, relative humidity, DDR, and $\delta^{13}C_{org}$ series were detrended using a 35 % locally weighted scatterplot smoothing (LOWESS) detrending method to reduce long-term non-orbital trends. Spectral analyses were performed using Acycle 2.6 (M. Li et al., 2019). Dominant periodicities were identified using the multitaper method (MTM), and Gaussian band-pass filtering was applied to isolate the main orbital components (Weedon, 2003; Wang et al., 2011; Kodama and Hinnov, 2014; M. Li et al., 2019). Passbands of 0.11 ± 0.02 cycles m^{-1} and 1.11 ± 0.22 cycles m^{-1} were used for the Junggar and Ordos Basin records, respectively.

2.2.8 Climate model configuration

Climate simulations were carried out using the Community Earth System Model version 1.2.2 (CESM 1.2.2; Hurrell et al., 2013; Vertenstein et al., 2013) asynchronously coupled with the BIOME4 biogeography and biogeochemistry model (Kaplan et al., 2003). CESM 1.2.2 is a fully coupled atmosphere–ocean general circulation model, including atmosphere, land, ocean,

https://doi.org/10.5194/egusphere-2026-6582
Preprint. Discussion started: 9 November 2026
© Author(s) 2026. CC BY 4.0 License.

sea-ice, and runoff components. The atmospheric component Community Atmosphere Model (CAM4) was run at a horizontal resolution of 3.75° × 3.75° with 26 vertical levels, while Community Land Model (CLM4.0) used the same horizontal grid with 10 vertical levels. The ocean component Parallel Ocean Program (POP2) and sea-ice component Los Alamos Sea Ice Model (CICE4) were run at nominal 3° resolution, and the runoff component was run at 0.5° × 0.5° resolution.

The paleogeographic boundary condition was based on the ~170 Ma reconstruction of Scotese and Wright (2018). The solar constant was reduced to 1342.49 W m^{-2} to account for lower Middle Jurassic solar luminosity (Gough, 1981). Atmospheric CH_4 and N_2O concentrations were set to 760 ppbv and 270 ppbv, respectively, without chlorofluorocarbons (CFCs); other atmospheric constituents followed preindustrial values, except for the prescribed CO_2 levels. Initial conditions were adopted from previous deep-time simulations (X. Li et al., 2022).

Three experiments were designed to isolate the effects of eccentricity and atmospheric CO_2. The control experiment C450_Se used pCO_2 = 450 ppmv and low eccentricity e = 0.0066. Experiment C450_Le used the same CO_2 level but high eccentricity e = 0.066, allowing the climatic effect of eccentricity to be assessed from the C450_Le − C450_Se contrast. Experiment C700_Se used pCO_2 = 700 ppmv and low eccentricity, so that the C700_Se − C450_Se contrast represents the effect of increased atmospheric CO_2. In all experiments, obliquity was fixed at 23.45°, and the longitude of perihelion was set to 270°, placing Northern Hemisphere summer solstice at perihelion. The experimental configurations are summarized in Table S1.

Because CESM 1.2.2 has limitations in representing deep-time vegetation distributions, it was asynchronously coupled with BIOME4 to provide vegetation fields during the simulations. Vegetation–climate coupling was updated every 40 model years and should not be interpreted as a fully dynamic vegetation module. The BIOME4 outputs are not treated here as an independent line of evidence; the analyses below focus primarily on simulated surface temperature and precipitation. Experiments C450_Se and C450_Le were run for 3600 model years, whereas C700_Se was run for 4600 model years. The last 100 years of each experiment were used for analysis after the modeled surface climate reached quasi-equilibrium.

3 Results and discussion

3.1 Types of coal-bearing peatlands and provenance of ash components

Because ancient dust reconstructions from coal-bearing successions can be compromised by fluvial clastic input, we first evaluated whether the studied peatlands were directly influenced by river-channel or overbank sediment supply. Coal-facies parameters indicate that the Junggar and Ordos peatlands were ombrotrophic. GWI values are consistently <1, and ash yields are generally <10 % (Figs. 2, S1, S2), consistent with ombrotrophic mires in which mineral input is largely isolated from groundwater and surface-water influence (Clymo, 1987; Diessel, 2007). In addition, no obvious channel-related coarse-grained interbeds, erosive bases, or clastic partings were observed within the sampled coal intervals. These features suggest that direct riverine detrital input into the studied peatlands was limited.

https://doi.org/10.5194/egusphere-2026-6582
Preprint. Discussion started: 9 November 2026
© Author(s) 2026. CC BY 4.0 License.

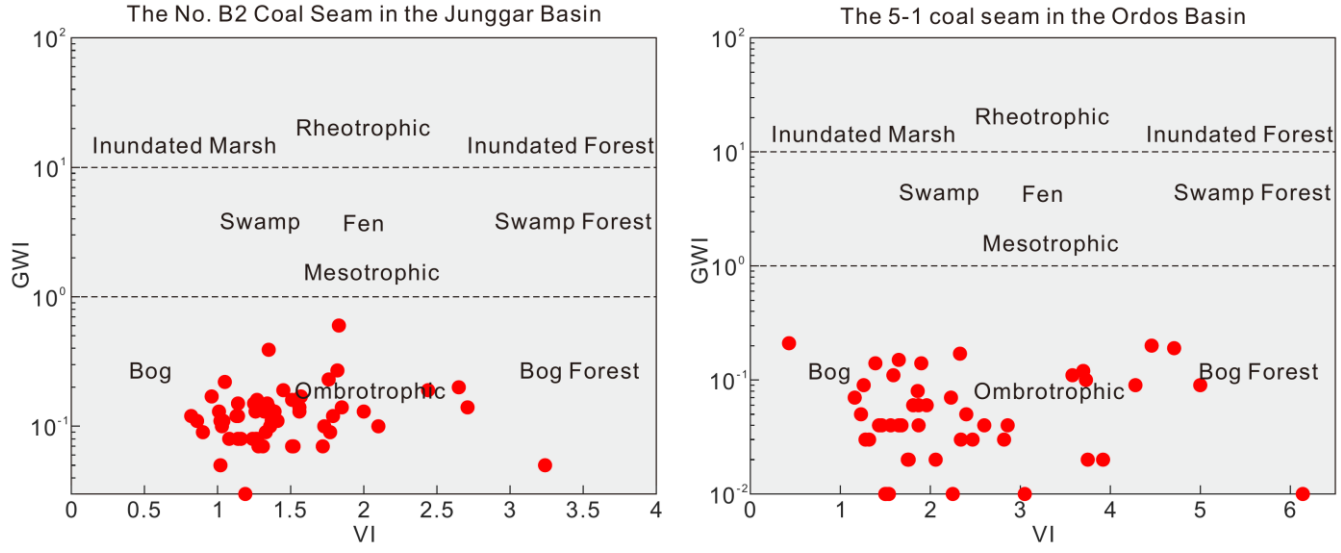


Figure 2. VI *vs.* GWI plots showing hydrological and paleodepositional conditions (modified from Calder et al., 1991).

Geochemical data further characterize the provenance of the mineral matter preserved in the coal seams (Fig. S3). In the Xishanyao Formation, 27 of 58 coal samples plot within the intermediate-source field and another 27 within the felsic-source field, whereas four samples fall outside these two principal fields. In contrast, 13 of 16 published coeval clastic-rock samples plot within the intermediate-source field and only three within the felsic-source field. The contrasting proportions of intermediate- and felsic-source affinities suggest differences in provenance composition between the coal-hosted mineral matter and the regional clastic sediments.

Trace-element ratios show a consistent but more dispersed pattern. The Xishanyao coal samples exhibit a broader La/Sc distribution than the coeval clastic rocks, although overlap occurs in both La/Sc and Co/Th (Fig. S3c). A comparable pattern occurs in the Yan'an Formation, where the regional sandstone samples yield La/Sc values of 1.71–3.57 and Co/Th values of 0.76–2.99, whereas the coal samples display substantially broader compositional ranges (Fig. S3d). These differences indicate that the mineral matter preserved in the coal seams does not simply reproduce the provenance distribution represented by the regional clastic sediments. Because these geochemical indicators primarily constrain source-rock composition rather than transport mechanism, they do not independently demonstrate aeolian deposition. However, together with the ombrotrophic coal-facies characteristics, generally low ash yields, and absence of channel-related clastic interbeds, they argue against dominant direct riverine supply.

Detrital zircon U–Pb ages provide an additional provenance constraint in both basins. In the Junggar Basin, detrital zircons extracted from coal samples of the No. B2 coal seam in the Xishanyao Formation show mixed age populations at ca. 171, 297, 333, 441, and 518 Ma (Fig. 3a), whereas coeval fluvial sandstones in eastern Junggar are dominated by Carboniferous peaks at ~328–340 Ma (Fig. 3b; Liu et al., 2024). This contrast suggests limited clastic input from nearby basin-margin sources. Furthermore, although a small number of zircon grains yield ages concentrated at ~171 Ma, their high euhedrality and well-

https://doi.org/10.5194/egusphere-2026-6582
Preprint. Discussion started: 9 November 2026
© Author(s) 2026. CC BY 4.0 License.

developed oscillatory zoning may indicate local magmatic activity near the peat-forming area (F. Wang et al., 2022), thus providing a crucial chronostratigraphic anchor for the No. B2 coal seam. However, the analyzed stratigraphic section shows that the thick coal seam is highly continuous, with no identifiable tonstein layers or distinct volcanic ash partings observed. This suggests extremely low volcanic ash input during atmospheric dust accumulation and that volcanic activity had a limited influence on the peat-forming system. In contrast, the dispersed zircon age spectrum is consistent with a mixed distal source signature, supporting the persistent supply of long-distance aeolian dust to the peat-forming environment.

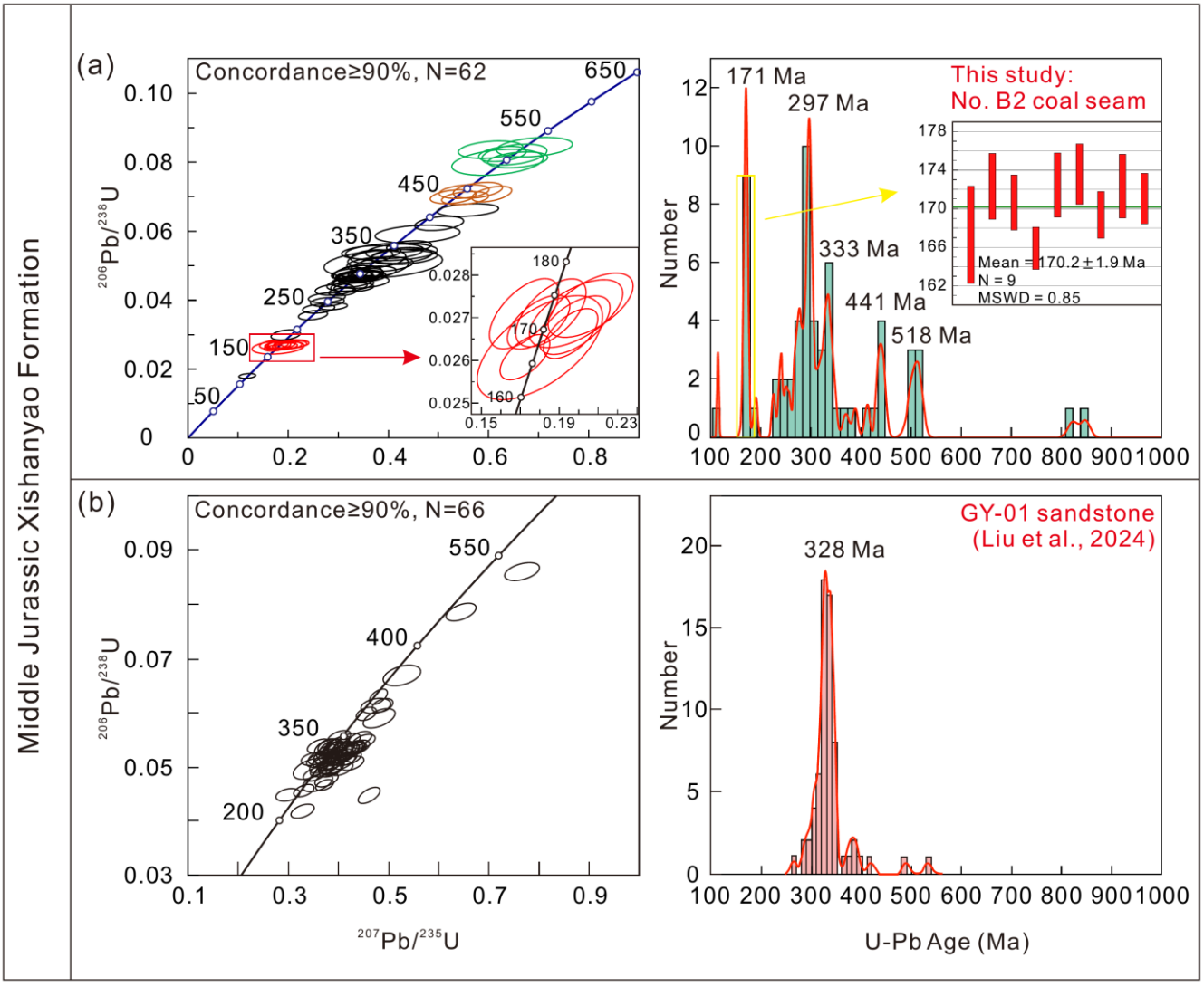
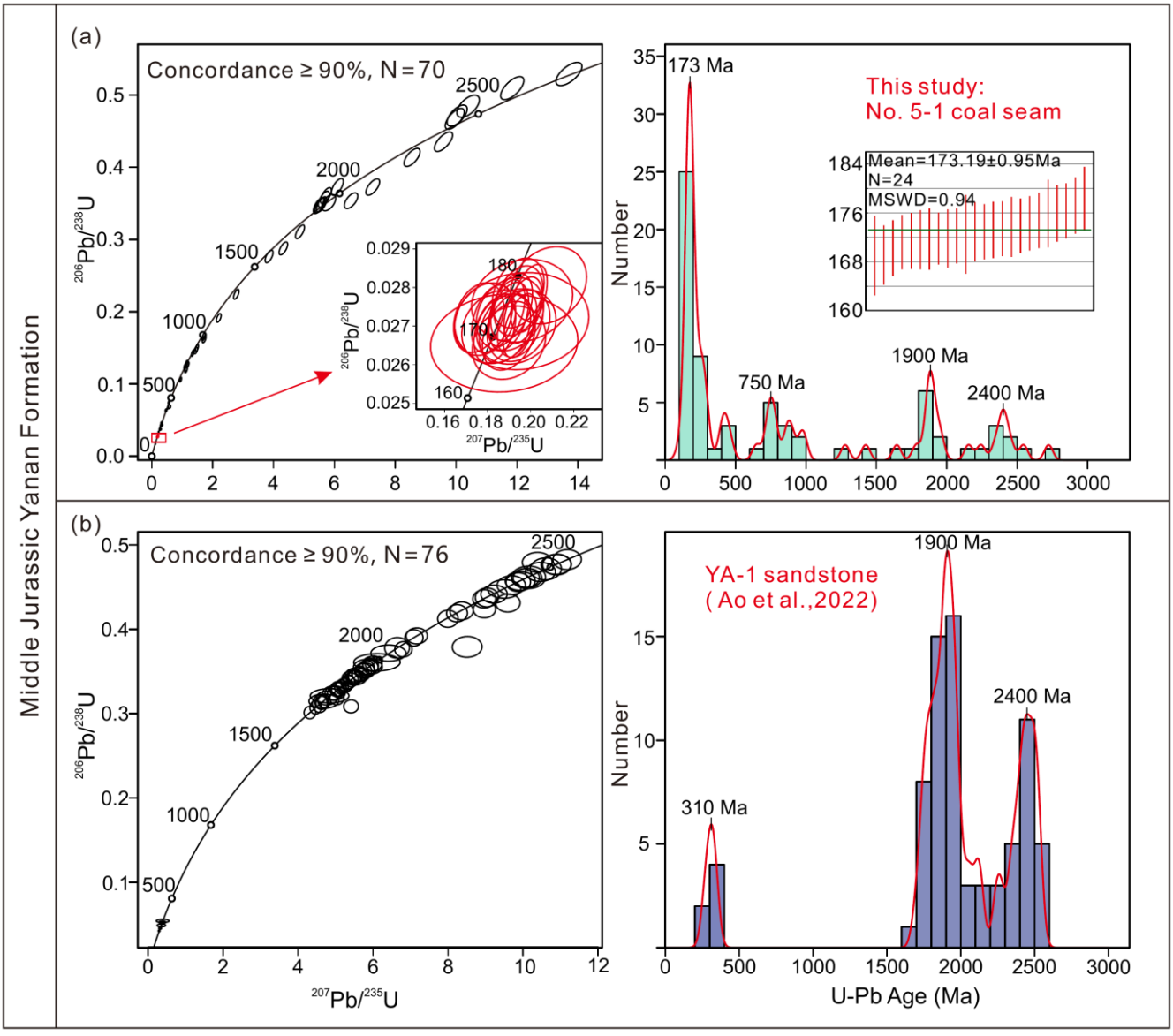


Figure 3. Detrital-zircon U–Pb results from the Middle Jurassic Xishanyao Formation in the Junggar Basin. (a) Concordia diagram and age-frequency distribution for zircons extracted from the No. B2 coal seam. The inset in the Concordia diagram enlarges the youngest zircon population, and the inset in the age-frequency diagram shows its weighted mean $^{206}Pb/^{238}U$ age of 170.2 ± 1.9 Ma (*N* = 9, mean square of weighted deviates (MSWD) = 0.85). (b) Concordia diagram and age-frequency distributions for the coeval GY-01 fluvial sandstones; sandstone data are from Liu et al. (2024).

https://doi.org/10.5194/egusphere-2026-6582
Preprint. Discussion started: 9 November 2026
© Author(s) 2026. CC BY 4.0 License.



225 **Figure 4. Detrital-zircon U–Pb results from the Middle Jurassic Yan'an Formation in the Ordos Basin. (a) Concordia diagram and age-frequency distribution for zircons extracted from the No. 5-1 coal seam. The inset in the Concordia diagram enlarges the youngest zircon population, and the inset in the age-frequency diagram shows its weighted mean $^{206}Pb/^{238}U$ age of 173.19 ± 0.95 Ma (N = 24, MSWD = 0.94). (b) Concordia diagram and age-frequency distribution for the YA-1 sandstone; sandstone data are from Ao et al. (2022).**

230 A comparable coal-sandstone contrast is observed in the Ordos Basin. Zircons from the No. 5-1 coal seam show a prominent Middle Jurassic population at ca. 173 Ma, with a weighted mean $^{206}Pb/^{238}U$ age of 173.19 ± 0.95 Ma (N = 24, MSWD = 0.94), together with subordinate older populations around ca. 750 Ma, 1.9 Ga, and 2.4 Ga (Fig. 4a). In contrast, the YA-1 sandstone is characterized mainly by populations at ca. 310 Ma, 1.9 Ga, and 2.4 Ga and lacks a comparably dominant Middle Jurassic

https://doi.org/10.5194/egusphere-2026-6582
Preprint. Discussion started: 9 November 2026
© Author(s) 2026. CC BY 4.0 License.

population (Fig. 4b; Ao et al., 2022). The shared Paleoproterozoic–Neoarchean populations indicate partial overlap in source terranes, whereas the markedly different relative age distributions, particularly the dominance of the ca. 173 Ma population in the coal, argue against simple derivation of the coal-hosted mineral matter from the regional fluvial sandstone detrital population.

Ash sources in coal are complex. In addition to detrital minerals delivered into the peat-forming mires by fluvial transport or atmospheric fallout (Bailey and Kosters, 1983; Triplehorn, 1990; Ruppert et al., 1991), they also include skeletal remains from plant materials, diatoms, and mollusks (Andrejko et al., 1983a, 1983b; Davis et al., 1984), as well as precipitates of authigenic, diagenetic, and epigenetic minerals (Spears and Caswell, 1986; Shotyk, 1988; Susilawati and Ward, 2006; Dawson et al., 2012). However, across several sources, minerals formed during plant development and skeletal particles of organisms are usually scarce (Ward, 2016), and we have not observed minerals such as thin films, veins, or other features indicative of epigenetic minerals in our samples. Therefore, biological, groundwater-related, or hydrothermal contributions to ash in the studied coal seams were likely minimal. Taken together, the low GWI values and ash yields, the absence of direct channel-related clastic input, the geochemical separation from coeval fluvial sediments, and the contrasting detrital-zircon age distributions indicate that direct riverine supply was limited in both peatlands. We therefore infer that the ash-forming mineral matter was predominantly supplied by atmospheric fallout, consistent with wind-mediated transport of mineral particles into the ombrotrophic peat-forming environments.

3.2 Climate-induced variations in peatland dust deposition

In this study, Middle Jurassic climatic evolution is reconstructed primarily from palynological records, including ecological affinities of parent plants, distributions of ecological plant groups, and sample scores from detrended correspondence analysis (DCA) (Baranyi et al., 2024). The vertical and horizontal DCA axes are interpreted to reflect relative temperature and humidity gradients based on the ecological affinities and climate preferences of dominant plant groups (Fig. 5). In addition, bulk organic carbon isotope composition ($\delta^{13}C_{org}$) provides complementary information regarding the stability of the terrestrial vegetation–climate system. Given that C_4-dominated ecosystems did not expand extensively until the Late Cenozoic (Edwards et al., 2010), and that our palynological assemblages are dominated by ferns and gymnosperms (Figs. 6, S4–S6), variations in bulk organic carbon isotopic composition ($\delta^{13}C_{org}$) are interpreted primarily as signals derived from a non-C_4 vegetation background. Although the possibility of alternative photosynthetic pathways, such as crassulacean acid metabolism (CAM), cannot be entirely excluded in deep-time ecosystems, $\delta^{13}C_{org}$ is used here only as a supplementary indicator of vegetation-climate system stability. Its variability may have responded in part to hydroclimatic fluctuations, but it is not treated as an independent or exclusive proxy for effective moisture. Because carbon-isotope fractionation in plants is influenced by both photosynthetic physiology and environmental conditions (O'Leary, 1988; Farquhar et al., 1989), and because the overall amplitude of $\delta^{13}C_{org}$ variation is limited (Fig. S2), the record suggests that no major abrupt climatic perturbation or ecological reorganization occurred during peat accumulation. Such relatively stable background conditions likely favored the preservation of orbitally paced environmental signals in both the vegetation and sedimentary records.

https://doi.org/10.5194/egusphere-2026-6582
Preprint. Discussion started: 9 November 2026
© Author(s) 2026. CC BY 4.0 License.

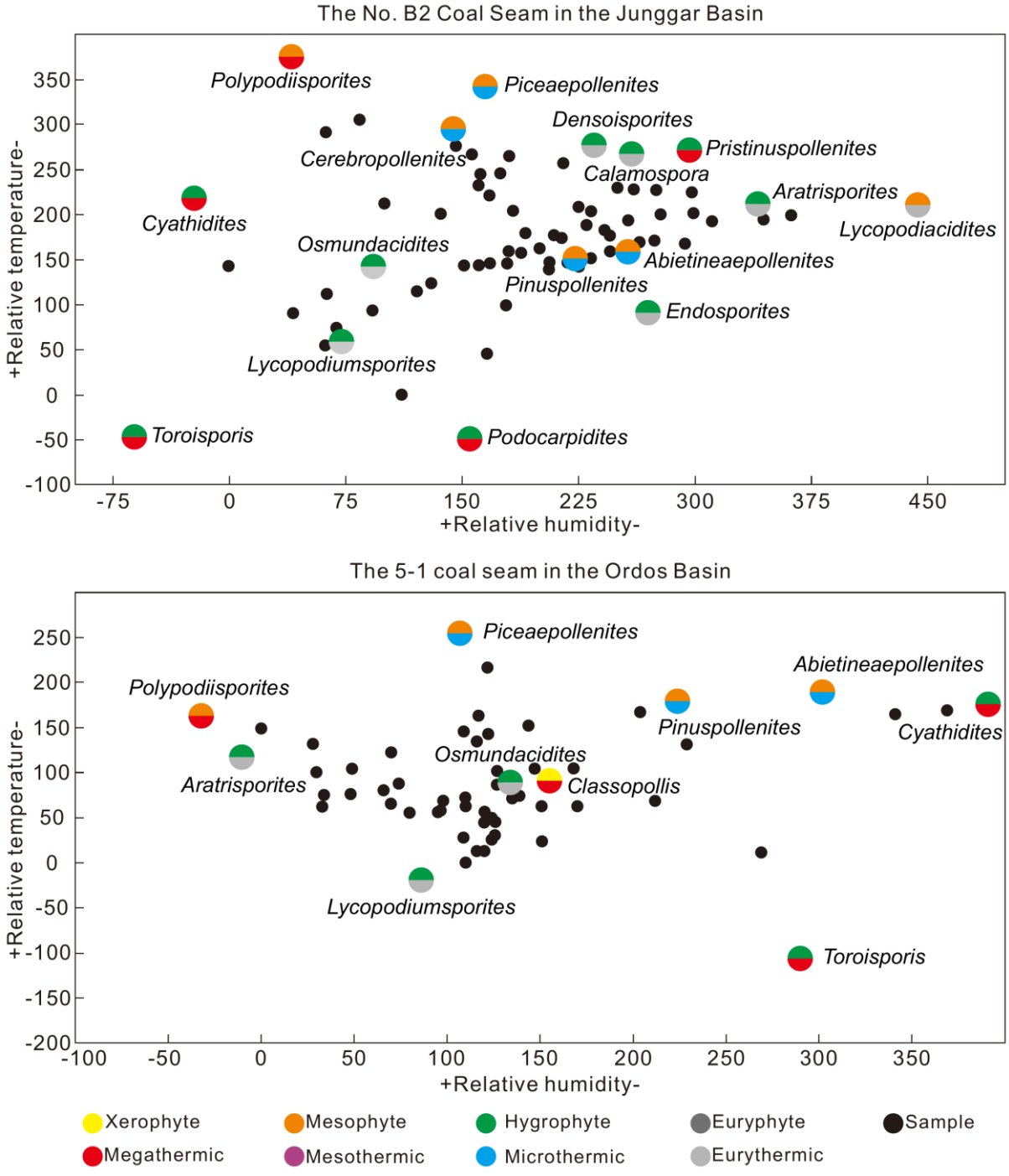


Figure 5. Detrended correspondence analysis (DCA) ordination plot of palynological samples from the No. B2 coal seam in the Junggar Basin and the No. 5-1 coal seam in the Ordos Basin.

https://doi.org/10.5194/egusphere-2026-6582
Preprint. Discussion started: 9 November 2026
© Author(s) 2026. CC BY 4.0 License.

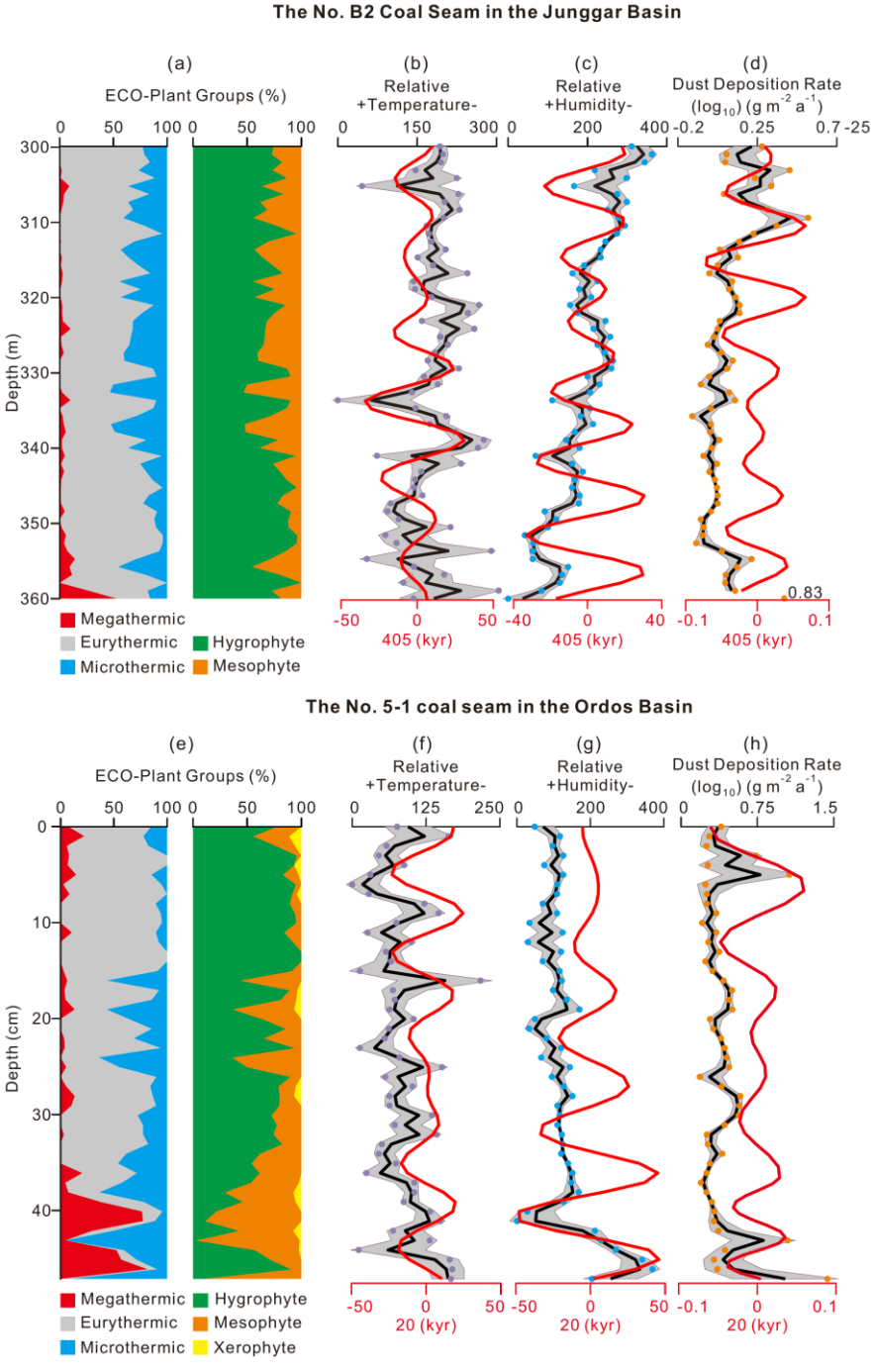


Figure 6. Paleovegetation, palynoclimate and peatland dust deposition rate of coal seams in the Junggar and Ordos basins. (a, e) Relative percentages of eco-plant sporopollen groups; (b, c, f, g) DCA-derived temperature-axis and humidity-axis scores; (d, h) Dust deposition rates in the peatlands.

https://doi.org/10.5194/egusphere-2026-6582
Preprint. Discussion started: 9 November 2026
© Author(s) 2026. CC BY 4.0 License.

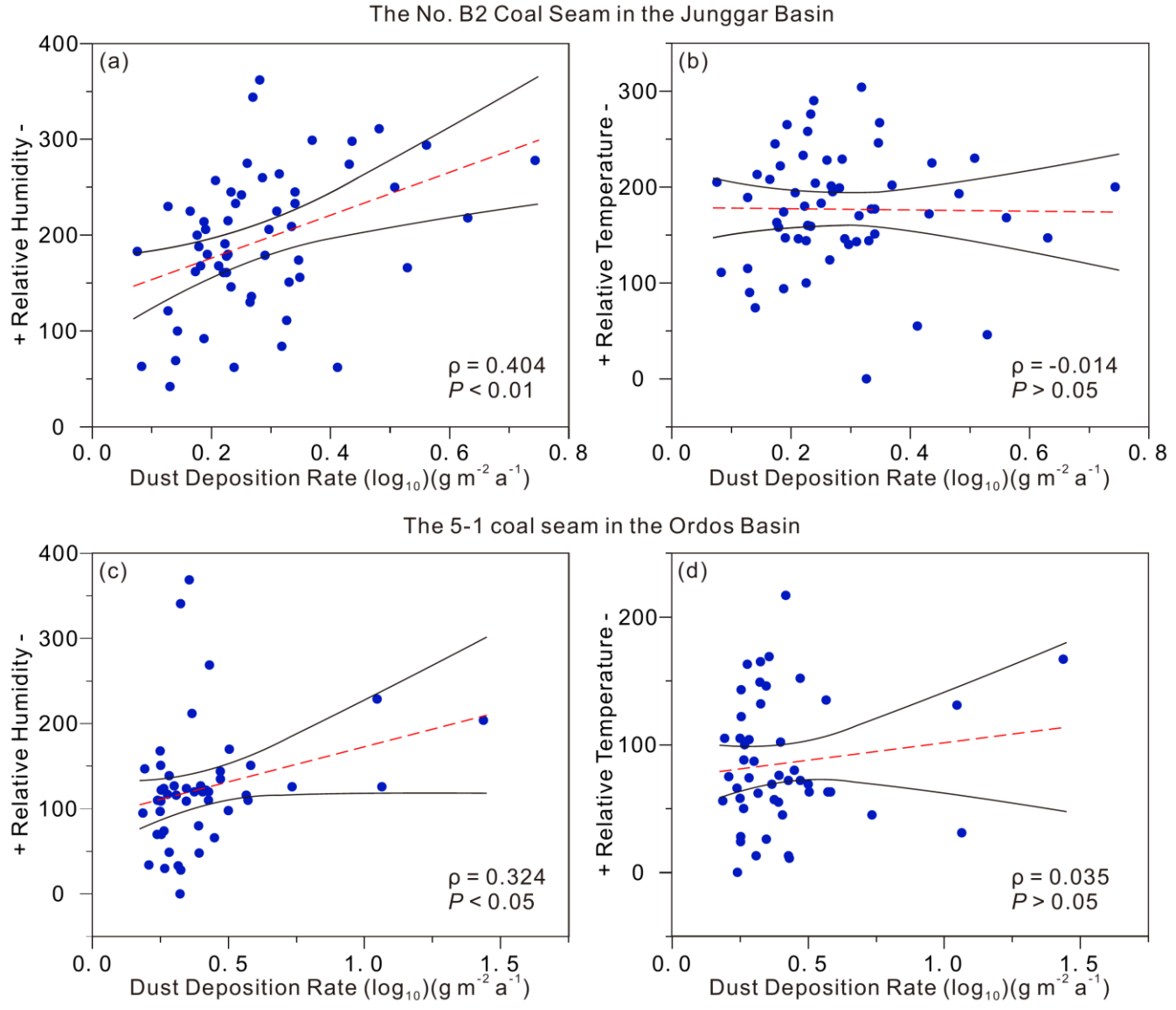


Figure 7. Cross-plots of DCA-derived climatic indicators and dust deposition rates for the No. B2 coal seam in the Junggar Basin and the No. 5-1 coal seam in the Ordos Basin. (a, c) Humidity-axis scores versus dust deposition rate; higher humidity-axis scores indicate drier conditions. (b, d) Temperature-axis scores versus dust deposition rate; higher temperature-axis scores indicate relatively cooler conditions. The red line denotes the best-fit linear regression line. The black curves denote the 95 % confidence interval.

Calculations indicate atmospheric dust deposition rates of 0.76–6.73 (mean 1.37) g m^{-2} a^{-1} and 1.53–27.36 (mean 3.26) g m^{-2} a^{-1} for the Middle Jurassic peatlands in the Xishanyao Formation of the Junggar Basin and Yan'an Formation of the Ordos Basin, respectively (Figs. 6d, h). DDR shows significant positive correlations with DCA humidity-related axis scores [Junggar Basin: Spearman's ρ = +0.404, P < 0.01; Ordos Basin: Spearman's ρ = +0.324, P < 0.05; Figs. 7a, c], for which higher scores indicate drier conditions. In contrast, correlations between DDR and DCA-derived temperature scores are negligible [Junggar

https://doi.org/10.5194/egusphere-2026-6582
Preprint. Discussion started: 9 November 2026
© Author(s) 2026. CC BY 4.0 License.

Basin: Spearman's $\rho = -0.014$, $P > 0.05$; Ordos Basin: Spearman's $\rho = +0.035$, $P > 0.05$; Figs. 7b, d]. Specifically, intervals of reduced humidity, as indicated by xerophytic plant dominance and DCA sample scores, coincide with elevated DDR, indicating that humidity was an important factor influencing dust accumulation.

The inverse relationship between humidity and DDR probably results from climatic factors controlling the regional dust cycle. Humid conditions can stabilize dust-source areas by increasing soil moisture and vegetation cover, thereby reducing dust emission (Prospero et al., 2002). In addition, higher precipitation enhances atmospheric wet scavenging, a process in which falling raindrops remove suspended mineral particles from the atmosphere. Collectively, these mechanisms reasonably explain the reduction in atmospheric dust loading and the decline in dust deposition rate in peatlands during humid intervals.

In addition, the atmospheric dust deposition rate in the Ordos Basin was significantly higher than that in the Junggar Basin. This discrepancy is consistent with climate simulation results (Fig. S7), which show that the Ordos Basin was located closer to the arid zone with scarce precipitation. Vegetation reconstruction data further support this interpretation, with the Junggar Basin dominated by hygrophytes and mesophytes, whereas the Ordos Basin developed a distinctive xerophytic vegetation community (Figs. 6a, e).

3.3 Orbital forcing of peatland dust deposition and its implications

Spectral analysis and band-pass filtering of the atmospheric dust deposition rate (DDR), relative humidity, and associated climatic proxy series reveal a ~405 kyr long eccentricity cycle in the Junggar Basin and a ~20 kyr precession cycle in the Ordos Basin (Figs. S8, S9). This difference in dominant periodicities primarily reflects variations in stratigraphic thickness and sampling resolution (Weedon, 2003; Hinnov, 2013). The ~60 m thick B2 coal seam in the Junggar Basin favors the preservation of long-period orbital variability, whereas high-resolution sampling (10 cm interval) in the Ordos Basin captures higher-frequency precession variability. The ~100 kyr short eccentricity signal is comparatively weak or absent, a pattern commonly attributed to sedimentary filtering and variations in accumulation rate that preferentially preserve longer orbital cycles (Hinnov, 2000; Meyers, 2015). In contrast, the ~405 kyr cycle is widely recognized as the most stable orbital tuning component (Laskar et al., 2004). In addition, the stronger ~20 kyr signal in the Ordos Basin may also partly reflect regional differences in hydroclimatic sensitivity to orbital forcing. Precession commonly exerts a strong influence on low- to mid-latitude seasonal insolation and associated hydroclimatic seasonality, whereas eccentricity mainly modulates the amplitude of precession-driven climate variability. However, given the available data, this interpretation remains tentative, and the observed basin-scale difference is more directly supported by differences in stratigraphic architecture, sampling resolution, and depositional filtering (Kutzbach, 1981; Laskar et al., 2004; Merlis et al., 2013).

https://doi.org/10.5194/egusphere-2026-6582
Preprint. Discussion started: 9 November 2026
© Author(s) 2026. CC BY 4.0 License.

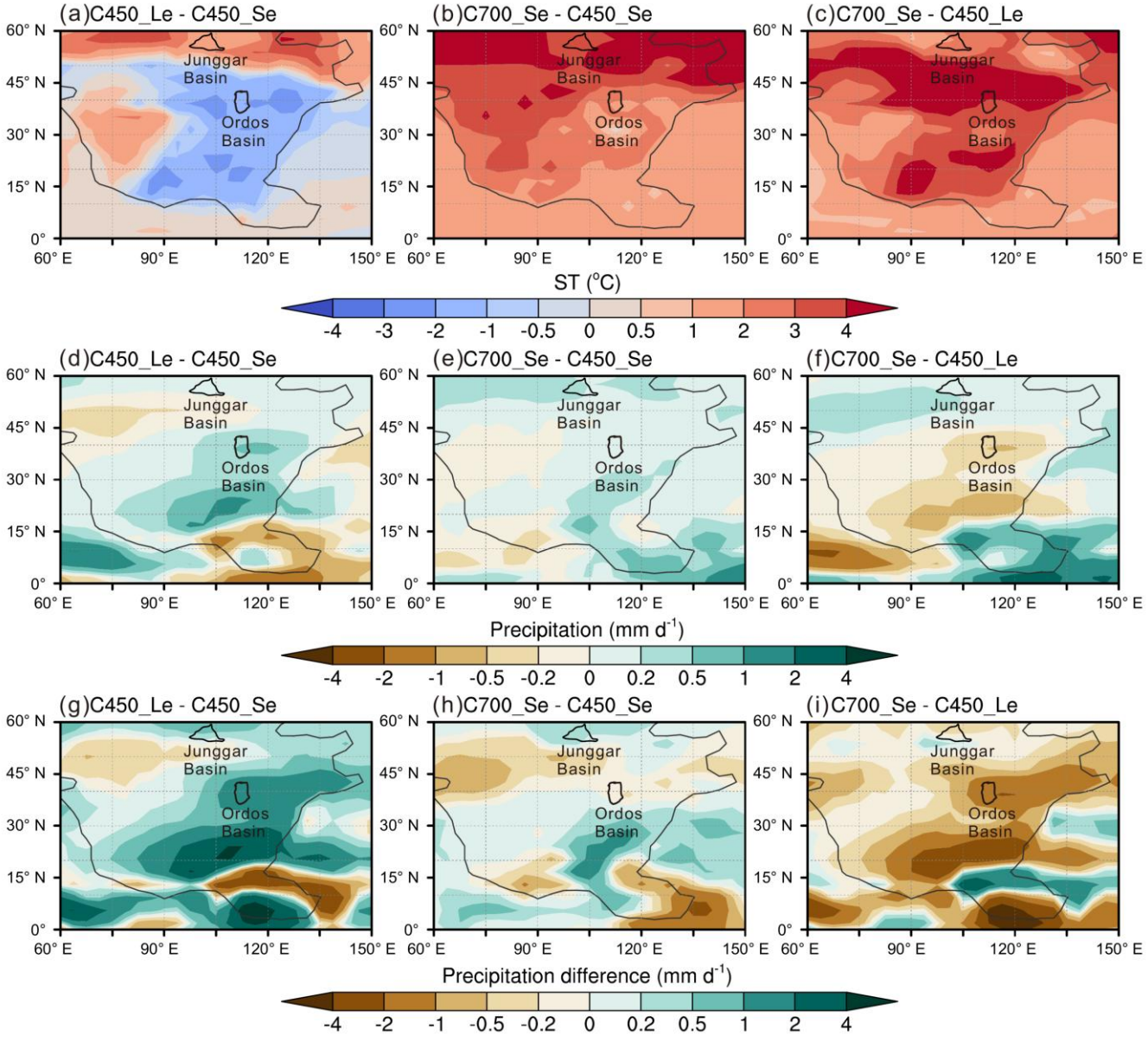


Figure 8. Simulated responses of regional Northern Hemisphere climate to changes in eccentricity and pCO_2 during the Middle Jurassic. (a–c) Surface temperature (ST), (d–f) precipitation, and (g–i) summer-winter precipitation difference, calculated as mean June–August precipitation minus mean November-January precipitation. C450 and C700 indicate pCO_2 levels of 450 and 700 ppmv, respectively; Le and Se indicate high- and low-eccentricity conditions, respectively. Panel labels show the anomalies between paired experiments.

To further investigate the influence of astronomical orbital forcing on precipitation seasonality, we conducted climate simulations for the Middle Jurassic. The simulations indicate that orbital forcing strongly influenced hydroclimatic variability across China. Under scenarios with elevated pCO_2 and reduced eccentricity, precipitation variability exhibited an overall decreasing trend (Fig. 8i), and this pattern became more pronounced when only eccentricity forcing was considered (Fig. 8g),

https://doi.org/10.5194/egusphere-2026-6582
Preprint. Discussion started: 9 November 2026
© Author(s) 2026. CC BY 4.0 License.

indicating that eccentricity plays a key role in regulating precipitation seasonality. At the regional scale, the two basins showed distinct differences in their responses to orbital forcing. In the Junggar Basin, the simulations revealed relatively modest changes in annual mean precipitation, whereas seasonal precipitation variability decreased significantly under high pCO_2 and low eccentricity conditions. In contrast, the Ordos Basin displayed a more pronounced hydroclimatic response, characterized by increased surface temperature (Fig. 8c) but decreased annual precipitation and precipitation variability (Figs. 8f, i). Notably, the magnitude of changes in annual mean precipitation was relatively limited compared with that of precipitation variability, suggesting that orbital forcing primarily modified the seasonal distribution of precipitation rather than substantially altering total precipitation amounts. These model results are consistent with the study by Zhang et al. (2023) on the Ordos Basin, which documented that ~405 kyr eccentricity maxima coincided with reduced surface temperatures, reflecting strong seasonal climate variations induced by orbital forcing. Integrating climate simulations with geological records, we infer that orbital eccentricity modulated the amplitude of precession-driven insolation forcing, thereby indirectly influencing seasonal hydroclimatic variability. Dust transport may also have occurred within the broader context of mid-latitude westerly circulation (Zhong et al., 2024), although our data and simulations suggest hydroclimatic control through changes in humidity and precipitation seasonality.

A comparative analysis of peat dust deposition rates and palynological climatic proxies reveals a prominent anti-phase relationship between dust deposition rate and relative humidity at the ~405 kyr eccentricity and ~20 kyr precession scales (Figs. 6c, d, g, h). Orbital eccentricity modulates the amplitude of precession-driven insolation variations (Laskar et al., 2004, 2011). During eccentricity maxima, seasonal hydroclimatic variability in China is likely intensified, accompanied by increases in precipitation and vegetation coverage. This stabilizes potential dust source areas and suppresses dust emission (Fig. 9a). Conversely, intervals of low eccentricity correspond to drier climatic conditions, which favor enhanced dust entrainment and transport (Fig. 9b). The persistent inverse relationship between reconstructed humidity and DDR, together with coincident orbital-scale spectral peaks, supports a strong hydroclimatic influence on dust deposition, although contributions from changes in atmospheric circulation cannot be excluded. Changes in eco-plant community assemblages further support the interpretation that orbitally forced hydroclimatic fluctuations controlled regional dust deposition.

https://doi.org/10.5194/egusphere-2026-6582
Preprint. Discussion started: 9 November 2026
© Author(s) 2026. CC BY 4.0 License.

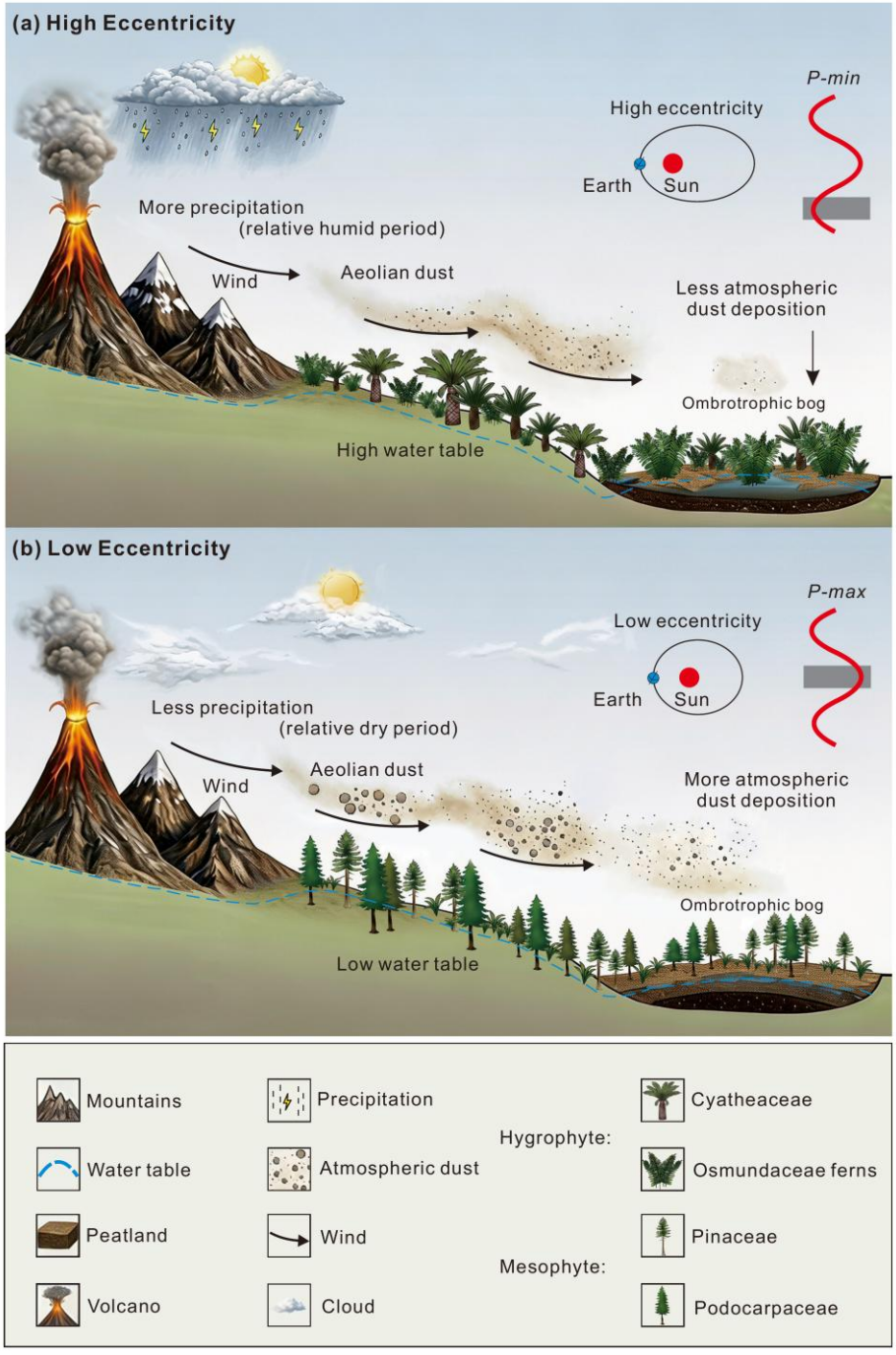


Figure 9. Conceptual model of orbital-scale dust deposition in Middle Jurassic peatlands. Humid phases paced by eccentricity and precession suppress dust deposition through increased precipitation and vegetation cover, whereas drier phases enhance dust accumulation.

https://doi.org/10.5194/egusphere-2026-6582
Preprint. Discussion started: 9 November 2026
© Author(s) 2026. CC BY 4.0 License.

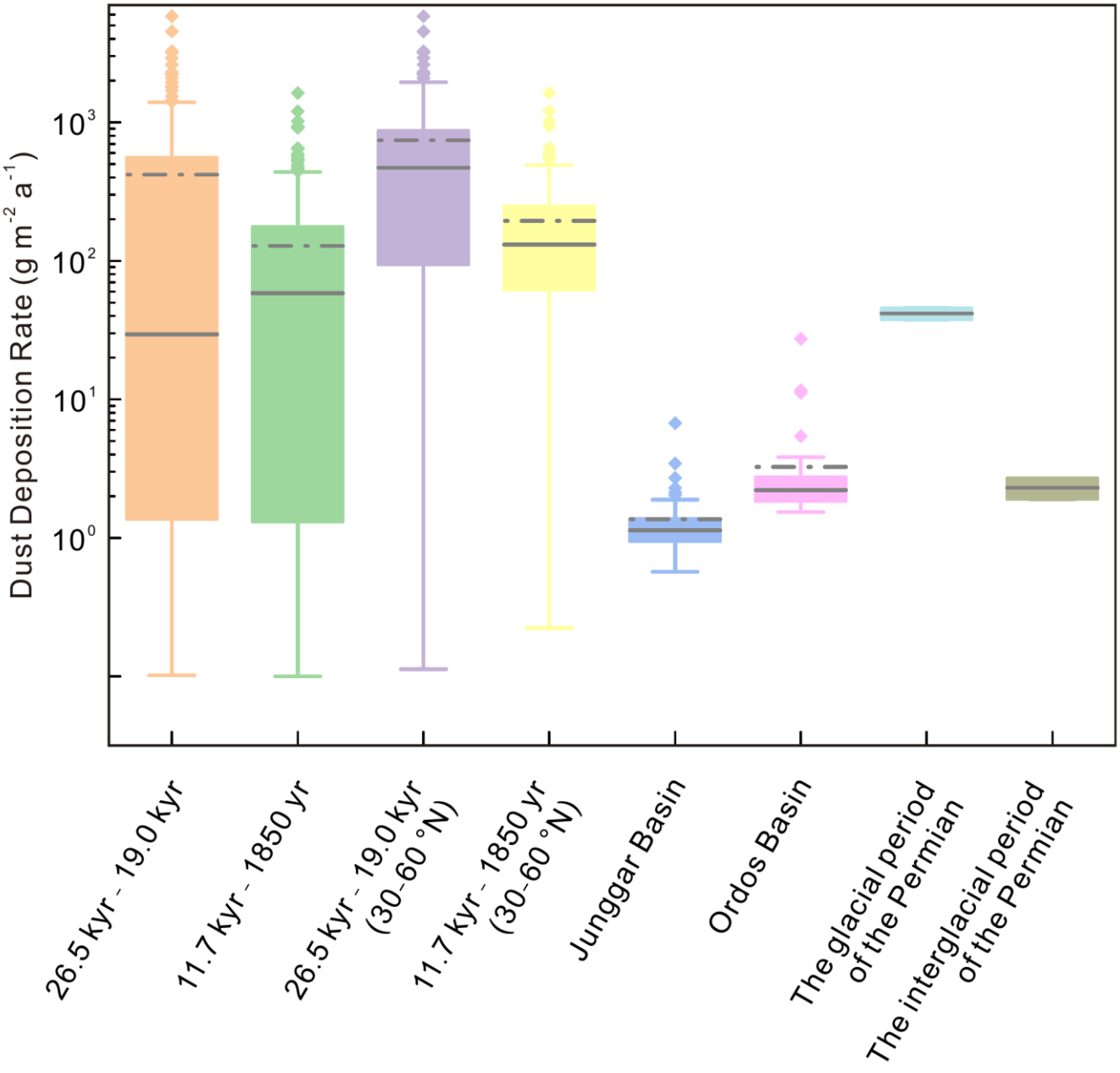


Figure 10. Comparison of atmospheric dust deposition rates among the Holocene, Jurassic, and Permian. Data compiled from Sardar Abadi et al. (2021) and Cosentino et al. (2024).

From a broader perspective, the reconstructed Middle Jurassic atmospheric dust deposition rates (DDR) in the Junggar and Ordos basins are markedly lower than those recorded for the Holocene and Late Paleozoic icehouse intervals (Fig. 10; Sardar Abadi et al., 2021; Cosentino et al., 2024). This contrast suggests that while orbital forcing controls high-frequency variability in dust flux, the global climatic background state ultimately determines the baseline intensity of the atmospheric dust cycle

https://doi.org/10.5194/egusphere-2026-6582
Preprint. Discussion started: 9 November 2026
© Author(s) 2026. CC BY 4.0 License.

(Pfeifer et al., 2025; Ge et al., 2026). During icehouse intervals, dust fluctuations were commonly influenced by glacial–interglacial cycles that affected temperature, aridity, vegetation cover, and the intensity of atmospheric circulation (Montañez and Poulsen, 2013; Sardar Abadi et al., 2021). Colder conditions generally promoted drier climates and sparser vegetation cover, while increased gustiness and stronger winds further enhanced dust emission and transport (Y. Li et al., 2019). By contrast, under the ice-free greenhouse conditions of the Middle Jurassic, orbital forcing likely influenced dust deposition more directly through hydrological processes, particularly changes in humidity, effective moisture, and precipitation seasonality. Under the Middle Jurassic greenhouse conditions, the studied basins experienced an intensified hydrological cycle and expanded vegetation coverage, with plant communities ranging from hygrophytes in the Junggar Basin to xerophytic assemblages in the Ordos Basin. Such conditions not only stabilized potential dust source areas but also enhanced atmospheric wet scavenging efficiency. These results indicate that dust-cycle responses in Middle Jurassic China were more directly modulated by orbital forcing of precipitation seasonality rather than by large-scale continental glaciation. These findings provide a deep-time perspective on the sensitivity of atmospheric dust cycles to climate warming.

4 Conclusions

Coal petrography, low ash yields, geochemical comparison with coeval fluvial clastic rocks, and detrital-zircon evidence indicate that the Aalenian ombrotrophic peatlands in the Junggar and Ordos basins mainly received atmospheric fallout, enabling reconstruction of relative Middle Jurassic dust deposition. Dust deposition rates are estimated between 0.76 and 6.73 g m^{-2} a^{-1} in the Junggar Basin, and from 1.53 to 27.36 g m^{-2} a^{-1} in the Ordos Basin. A significant negative correlation exists between dust deposition and relative humidity, but not temperature, indicating that moisture availability primarily controlled dust accumulation during the Middle Jurassic greenhouse conditions. Within the published astrochronologic frameworks, DDR covaries with palynologically inferred hydroclimatic variability at frequencies corresponding to ~405 kyr eccentricity in the Junggar Basin and ~20 kyr precession in the Ordos Basin, supporting orbital modulation of dust deposition through hydroclimatic variability. Climate simulations suggest orbital forcing affected dust dynamics mainly through changes in precipitation seasonality and hydroclimatic variability. In comparison to Holocene and Late Paleozoic icehouse records, the comparatively lower Middle Jurassic dust fluxes are consistent with the interpretation that greenhouse hydroclimatic conditions reduced overall dust emission intensity.

Data availability

The supporting data for this study are openly available in Mendeley Data (Ding, 2026), version 3, at https://doi.org/10.17632/nn5n3x6z2b.3. Third-party data used for comparisons and boundary conditions are cited in Sect. 2.2.3, Sect. 2.2.8, and the relevant figure captions.

https://doi.org/10.5194/egusphere-2026-6582
Preprint. Discussion started: 9 November 2026
© Author(s) 2026. CC BY 4.0 License.

Supplementary material

Supplementary material associated with this article contains Figs. S1–S9 and Table S1. Table S1 describes the Middle Jurassic paleoclimate modeling experiments.

Author contributions

Dawei Lv: Conceptualization, Methodology, Writing – review & editing.
Xinyi Ding: Data curation, Formal analysis, Visualization, Writing – original draft, Writing – review & editing.
Zhihui Zhang: Conceptualization, Supervision, Writing – review & editing.
Guibo Zheng: Investigation, Writing – review & editing.
Mehrdad Sardar Abadi: Methodology, Writing – review & editing.
Jian Zhang: Investigation, Formal analysis, Writing – review & editing.
Zicheng Yu: Writing – review & editing.
Chengshan Wang: Writing – review & editing.
Munira Raji: Writing – review & editing.
Bing Wang: Investigation, Data curation, Formal analysis, Writing – review & editing.
Dawei Lv, Xinyi Ding, Zhihui Zhang, Guibo Zheng, Mehrdad Sardar Abadi, Jian Zhang, Zicheng Yu, Chengshan Wang, and Munira Raji contributed to the interpretation of the results. All authors discussed the results, reviewed the manuscript, and approved the final version.

Competing interests

The authors declare that they have no conflict of interest.

Financial support

This work is supported by the Deep Earth Probe and Mineral Resources Exploration, National Science and Technology Major Project of China (2024ZD1001105), the National Natural Science Foundation of China (42472165), and the Youth Innovation Team Development Program of Institutions of Higher Education in Shandong Province (2024KJG034).

https://doi.org/10.5194/egusphere-2026-6582
Preprint. Discussion started: 9 November 2026
© Author(s) 2026. CC BY 4.0 License.

References

Andrejko, M. J., Cohen, A. D., and Raymond Jr., R.: Origin of mineral matter in peat, in: Mineral Matter in Peat: Its Occurrence, Form, and Distribution, edited by: Raymond Jr., R. and Andrejko, M. J., Los Alamos National Laboratory Report LA-9907-OBES, Los Alamos, NM, 3–24, 1983a.

Andrejko, M. J., Raymond Jr., R., and Cohen, A. D.: Biogenic silica in peats: Possible source for chertification in lignites, in: Mineral Matter in Peat: Its Occurrence, Form, and Distribution, edited by: Raymond Jr., R. and Andrejko, M. J., Los Alamos National Laboratory Report LA-9907-OBES, Los Alamos, NM, 25–37, 1983b.

Ao, C., Cheng, Y., Tang, Y., Wang, S., Teng, X., Jin, R., Zhang, T., Xu, Z., Yang, J., Zhang, C., and Wang, S.: Detrital zircon analysis of the Mesozoic strata in the northern Ordos Basin: Revealing the source-to-sink relationships and tectonic settings, Geol. J., 57, 3251–3266, https://doi.org/10.1002/gj.4472, 2022.

ASTM International: Standard test method for ash in the analysis sample of coal and coke from coal, ASTM D3174-12(2018), https://doi.org/10.1520/D3174-12R18, 2018.

Bai, Y., Liu, B., and Li, H.: Geochemical characteristics of green sandstones in Mesozoic uranium-bearing strata in the northern Ordos Basin and their implications, Uranium Geol., 41, 13–28, (in Chinese with English abstract), https://doi.org/10.3969/j.issn.1000-0658.2025.41.002, 2025.

Bailey, A. and Kosters, E. C.: Silicate minerals in organic-rich Holocene deposits in southern Louisiana, in: Mineral Matter in Peat: Its Occurrence, Form, and Distribution, edited by: Raymond Jr., R. and Andrejko, M. J., Los Alamos National Laboratory Report LA-9907-OBES, Los Alamos, NM, 39–51, 1983.

Baranyi, V., Jin, X., Dal Corso, J., Li, B., and Kemp, D. B.: Vegetation response to climate change during an Early Jurassic hyperthermal event (Jenkyns Event) from Northern China (Ordos Basin), Palaeogeogr. Palaeoclimatol. Palaeoecol., 643, 112180, https://doi.org/10.1016/j.palaeo.2024.112180, 2024.

Bian, W., Hornung, J., Liu, Z., Wang, P., and Hinderer, M.: Sedimentary and palaeoenvironmental evolution of the Junggar Basin, Xinjiang, Northwest China, Palaeobiodivers. Palaeoenviron., 90, 175–186, https://doi.org/10.1007/s12549-010-0038-9, 2010.

Calder, J. H., Gibling, M. R., and Mukhopadhyay, P. K.: Peat formation in a Westphalian B piedmont setting, Cumberland Basin, Nova Scotia: Implications for the maceral-based interpretation of rheotrophic and raised paleomires, Bull. Soc. Géol. Fr., 162, 283–298, 1991.

Cao, M., Wang, Z., Sui, Y., Li, Y., Zhang, Z., Xiao, A., Zhang, R., and Kemp, D. B.: Mineral dust coupled with climate-carbon cycle on orbital timescales over the past 4 Ma, Geophys. Res. Lett., 48, e2021GL095327, https://doi.org/10.1029/2021GL095327, 2021.

Clymo, R. S.: Rainwater-fed peat as a precursor of coal, Geol. Soc. Lond. Spec. Publ., 32, 17–23, https://doi.org/10.1144/GSL.SP.1987.032.01.03, 1987.

https://doi.org/10.5194/egusphere-2026-6582
Preprint. Discussion started: 9 November 2026
© Author(s) 2026. CC BY 4.0 License.

Cosentino, N. J., Torre, G., Lambert, F., Albani, S., De Vleeschouwer, F., and Bory, A. J.-M.: Paleo±Dust: Quantifying uncertainty in paleo-dust deposition across archive types, Earth Syst. Sci. Data, 16, 941–959, https://doi.org/10.5194/essd-16-941-2024, 2024.

Davis, A., Russell, S. J., Rimmer, S. M., and Yeakel, J. D.: Some genetic implications of silica and aluminosilicates in peat and coal, Int. J. Coal Geol., 3, 293–314, https://doi.org/10.1016/0166-5162(84)90001-6, 1984.

Dawson, G. K. W., Golding, S. D., Esterle, J. S., and Massarotto, P.: Occurrence of minerals within fractures and matrix of selected Bowen and Ruhr Basin coals, Int. J. Coal Geol., 94, 150–166, https://doi.org/10.1016/j.coal.2012.01.004, 2012.

Diessel, C. F. K.: Utility of coal petrology for sequence-stratigraphic analysis, Int. J. Coal Geol., 70, 3–34, https://doi.org/10.1016/j.coal.2006.01.008, 2007.

Ding, X.: Supporting data for orbital-scale climate forcing of atmospheric dust flux in Middle Jurassic North China peatlands, version 3, Mendeley Data [data set], https://doi.org/10.17632/nn5n3x6z2b.3, 2026.

Edwards, E. J., Osborne, C. P., Strömberg, C. A. E., Smith, S. A., and C4 Grasses Consortium: The origins of C4 grasslands: Integrating evolutionary and ecosystem science, Science, 328, 587–591, https://doi.org/10.1126/science.1177216, 2010.

Fang, Y., Wu, C., Wang, Y., Hou, K., and Guo, Z.: Topographic evolution of the Tianshan Mountains and their relation to the Junggar and Turpan Basins, Central Asia, from the Permian to the Neogene, Gondwana Res., 75, 47–67, https://doi.org/10.1016/j.gr.2019.03.020, 2019.

Farquhar, G. D., Ehleringer, J. R., and Hubick, K. T.: Carbon isotope discrimination and photosynthesis, Annu. Rev. Plant Physiol. Plant Mol. Biol., 40, 503–537, https://doi.org/10.1146/annurev.pp.40.060189.002443, 1989.

Ge, Y., Sonke, J. E., Laffont, L., Them II, T. R., Bekker, A., and Wen, H.: Distal marine mercury signals in peak Late Paleozoic Ice Age: Implications for aeolian versus volcanic inputs, Geophys. Res. Lett., 53, e2026GL122666, https://doi.org/10.1029/2026GL122666, 2026.

General Administration of Quality Supervision, Inspection and Quarantine of the People's Republic of China: Determination of total organic carbon in sedimentary rock, GB/T 19145-2003, https://openstd.samr.gov.cn/bzgk/std/newGbInfo?hcno=36874ABBF6B21A5BF28627F45B75FDCE (last access: 25 October 2026), 2003.

General Administration of Quality Supervision, Inspection and Quarantine of the People's Republic of China and Standardization Administration of the People's Republic of China: Determination of apparent relative density of coal, GB/T 6949-2010, https://openstd.samr.gov.cn/bzgk/std/newGbInfo?hcno=B4EE76D5D3F1CE6A9665B047EF119E6F (last access: 25 October 2026), 2011.

Gough, D. O.: Solar interior structure and luminosity variations, Sol. Phys., 74, 21–34, https://doi.org/10.1007/BF00151270, 1981.

Hammer, Ø., Harper, D. A. T., and Ryan, P. D.: PAST: Paleontological statistics software package for education and data analysis, Palaeontol. Electron., 4(1), 4, 9 pp, https://palaeo-electronica.org/2001_1/past/past.pdf, 2001.

https://doi.org/10.5194/egusphere-2026-6582
Preprint. Discussion started: 9 November 2026
© Author(s) 2026. CC BY 4.0 License.

Hayashi, K.-I., Fujisawa, H., Holland, H. D., and Ohmoto, H.: Geochemistry of ~1.9 Ga sedimentary rocks from northeastern Labrador, Canada, Geochim. Cosmochim. Acta, 61, 4115–4137, https://doi.org/10.1016/S0016-7037(97)00214-7, 1997.

Hinnov, L. A.: New perspectives on orbitally forced stratigraphy, Annu. Rev. Earth Planet. Sci., 28, 419–475, https://doi.org/10.1146/annurev.earth.28.1.419, 2000.

Hinnov, L. A.: Cyclostratigraphy and its revolutionizing applications in the Earth and planetary sciences, Geol. Soc. Am. Bull., 125, 1703–1734, https://doi.org/10.1130/B30934.1, 2013.

Hurrell, J. W., Holland, M. M., Gent, P. R., Ghan, S., Kay, J. E., Kushner, P. J., Lamarque, J.-F., Large, W. G., Lawrence, D., Lindsay, K., Lipscomb, W. H., Long, M. C., Mahowald, N., Marsh, D. R., Neale, R. B., Rasch, P., Vavrus, S., Vertenstein, M., Bader, D., Collins, W. D., Hack, J. J., Kiehl, J., and Marshall, S.: The Community Earth System Model: A framework for collaborative research, Bull. Am. Meteorol. Soc., 94, 1339–1360, https://doi.org/10.1175/BAMS-D-12-00121.1, 2013.

International Committee for Coal and Organic Petrology: The new inertinite classification (ICCP system 1994), Fuel, 80, 459–471, https://doi.org/10.1016/S0016-2361(00)00102-2, 2001.

Jiang, X., Pan, Z., and Fu, Q.: Primary study on pattern of general circulation of atmosphere before uplift of the Tibetan Plateau in eastern Asia, Sci. China Ser. D-Earth Sci., 44, 680–688, https://doi.org/10.1007/BF02907197, 2001.

Jickells, T. D., An, Z. S., Andersen, K. K., Baker, A. R., Bergametti, G., Brooks, N., Cao, J. J., Boyd, P. W., Duce, R. A., Hunter, K. A., Kawahata, H., Kubilay, N., laRoche, J., Liss, P. S., Mahowald, N., Prospero, J. M., Ridgwell, A. J., Tegen, I., and Torres, R.: Global iron connections between desert dust, ocean biogeochemistry, and climate, Science, 308, 67–71, https://doi.org/10.1126/science.1105959, 2005.

Johnson, E. A., Liu, S., and Zhang, Y.: Depositional environments and tectonic controls on the coal-bearing Lower to Middle Jurassic Yan'an Formation, southern Ordos Basin, China, Geology, 17, 1123–1126, https://doi.org/10.1130/0091-7613(1989)017<1123:DEATCO>2.3.CO;2, 1989.

Kaplan, J. O., Bigelow, N. H., Prentice, I. C., Harrison, S. P., Bartlein, P. J., Christensen, T. R., Cramer, W., Matveyeva, N. V., McGuire, A. D., Murray, D. F., Razzhivin, V. Y., Smith, B., Walker, D. A., Anderson, P. M., Andreev, A. A., Brubaker, L. B., Edwards, M. E., and Lozhkin, A. V.: Climate change and Arctic ecosystems: 2. Modeling, paleodata-model comparisons, and future projections, J. Geophys. Res. Atmos., 108, 8171, https://doi.org/10.1029/2002JD002559, 2003.

Kent, D. V. and Irving, E.: Influence of inclination error in sedimentary rocks on the Triassic and Jurassic apparent pole wander path for North America and implications for Cordilleran tectonics, J. Geophys. Res. Solid Earth, 115, B10103, https://doi.org/10.1029/2009JB007205, 2010.

Kodama, K. P. and Hinnov, L. A.: Rock Magnetic Cyclostratigraphy, John Wiley & Sons, Ltd., Chichester, https://doi.org/10.1002/9781118561294, 2014.

Kutzbach, J. E.: Monsoon climate of the early Holocene: Climate experiment with the Earth's orbital parameters for 9000 years ago, Science, 214, 59–61, https://doi.org/10.1126/science.214.4516.59, 1981.

Laskar, J., Robutel, P., Joutel, F., Gastineau, M., Correia, A. C. M., and Levrard, B.: A long-term numerical solution for the insolation quantities of the Earth, Astron. Astrophys., 428, 261–285, https://doi.org/10.1051/0004-6361:20041335, 2004.

https://doi.org/10.5194/egusphere-2026-6582
Preprint. Discussion started: 9 November 2026
© Author(s) 2026. CC BY 4.0 License.

Laskar, J., Fienga, A., Gastineau, M., and Manche, H.: La2010: A new orbital solution for the long-term motion of the Earth, Astron. Astrophys., 532, A89, https://doi.org/10.1051/0004-6361/201116836, 2011.

Le Roux, G., Fagel, N., De Vleeschouwer, F., Krachler, M., Debaille, V., Stille, P., Mattielli, N., van der Knaap, W. O., van Leeuwen, J. F. N., and Shotyk, W.: Volcano- and climate-driven changes in atmospheric dust sources and fluxes since the Late Glacial in Central Europe, Geology, 40, 335–338, https://doi.org/10.1130/G32586.1, 2012.

Li, M., Hinnov, L., and Kump, L.: Acycle: Time-series analysis software for paleoclimate research and education, Comput. Geosci., 127, 12–22, https://doi.org/10.1016/j.cageo.2019.02.011, 2019.

Li, S.-L., Yu, X.-H., Tan, C.-P., Steel, R., and Hu, X.-F.: Jurassic sedimentary evolution of southern Junggar Basin: Implication for palaeoclimate changes in northern Xinjiang Uygur Autonomous Region, China, J. Palaeogeogr., 3, 145–161, https://doi.org/10.3724/SP.J.1261.2014.00049, 2014.

Li, X., Hu, Y., Guo, J., Lan, J., Lin, Q., Bao, X., Yuan, S., Wei, M., Li, Z., Man, K., Yin, Z., Han, J., Zhang, J., Zhu, C., Zhao, Z., Liu, Y., Yang, J., and Nie, J.: A high-resolution climate simulation dataset for the past 540 million years, Sci. Data, 9, 371, https://doi.org/10.1038/s41597-022-01490-4, 2022.

Li, Y., Song, Y., Qiang, M., Miao, Y., and Zeng, M.: Atmospheric dust variations in the Ili Basin, Northwest China, during the Last Glacial Period as revealed by a high mountain loess-paleosol sequence, J. Geophys. Res. Atmos., 124, 8449–8466, https://doi.org/10.1029/2019JD030470, 2019.

Li, Y., Yan, M., Liu, P., Lin, H., Li, S., Huo, S., and Yang, T.: Characteristics of the tectonic background and sedimentary paleoenvironment of coal-bearing strata from the Yan'an Formation in the Ordos Basin: Evidence from the geochemistry of major and trace elements, ACS Earth Space Chem., 6, 2680–2697, https://doi.org/10.1021/acsearthspacechem.2c00240, 2022.

Liu, M., Zhou, Y., Su, F., Yuan, Y. W., Zhu, Y. S., Xing, J. L., and Yang, Y. F.: U-Pb ages and Hf isotopic characteristics of the detrital zircon from Middle Jurassic sandstone in Santanghu Basin, eastern Junggar, and their significance to uranium mineralization, Geol. Rev., 70, 742–758, (in Chinese with English abstract), https://doi.org/10.16509/j.georeview.2023.10.032, 2024.

Liu, Y., Hu, Z., Gao, S., Günther, D., Xu, J., Gao, C., and Chen, H.: In situ analysis of major and trace elements of anhydrous minerals by LA-ICP-MS without applying an internal standard, Chem. Geol., 257, 34–43, https://doi.org/10.1016/j.chemgeo.2008.08.004, 2008.

Liu, Y., Gao, S., Hu, Z., Gao, C., Zong, K., and Wang, D.: Continental and oceanic crust recycling-induced melt-peridotite interactions in the Trans-North China Orogen: U-Pb dating, Hf isotopes and trace elements in zircons from mantle xenoliths, J. Petrol., 51, 537–571, https://doi.org/10.1093/petrology/egp082, 2010.

Lv, D., Shen, Y., van Loon, A. J. T., Raji, M., Zhang, Z., Song, G., Ren, Z., Wang, Y., and Wang, D.: Sequence stratigraphy of the Middle Jurassic Yan'an Formation (NE Ordos Basin, China), relationship with climate conditions and basin evolution, and coal maceral's characteristics, Front. Earth Sci., 10, 1086298, https://doi.org/10.3389/feart.2022.1086298, 2023.

https://doi.org/10.5194/egusphere-2026-6582
Preprint. Discussion started: 9 November 2026
© Author(s) 2026. CC BY 4.0 License.

Lv, D., Zheng, G., Zhang, Z., Lu, M., Raji, M., Mustapha, K. A., Wang, T., Wang, L., and Du, W.: Astronomically-forced wildfire control on high-latitude peatland carbon accumulation rate in the Middle Jurassic, Glob. Planet. Change, 253, 104906, https://doi.org/10.1016/j.gloplacha.2025.104906, 2025.

Marshall, C., Large, D. J., and Heavens, N. G.: Coal-derived rates of atmospheric dust deposition during the Permian, Gondwana Res., 31, 20–29, https://doi.org/10.1016/j.gr.2015.10.002, 2016.

Merlis, T. M., Schneider, T., Bordoni, S., and Eisenman, I.: The tropical precipitation response to orbital precession, J. Clim., 26, 2010–2021, https://doi.org/10.1175/JCLI-D-12-00186.1, 2013.

Meyers, S. R.: The evaluation of eccentricity-related amplitude modulation and bundling in paleoclimate data: An inverse approach for astrochronologic testing and time scale optimization, Paleoceanography, 30, 1625–1640, https://doi.org/10.1002/2015PA002850, 2015.

Montañez, I. P. and Poulsen, C. J.: The Late Paleozoic Ice Age: An evolving paradigm, Annu. Rev. Earth Planet. Sci., 41, 629–656, https://doi.org/10.1146/annurev.earth.031208.100118, 2013.

O'Leary, M. H.: Carbon isotopes in photosynthesis, BioScience, 38, 328–336, https://doi.org/10.2307/1310735, 1988.

Olsen, P. E., Sha, J., Fang, Y., Chang, C., Kent, D. V., Vajda, V., Whiteside, J. H., Kinney, S. T., Lampert, A., and MacLennan, S. A.: Empirical record, geochronology and theoretical determinates of Mesozoic climate in the Junggar Basin, NW China, in relation to other basins in NE China, in: The Triassic and Jurassic of the Junggar Basin, China: Advances in Palaeontology and Environments, edited by: Sha, J., Slater, S. M., Vajda, V., Olsen, P. E., and Zhang, H., Geol. Soc. Lond. Spec. Publ., 538, 235–260, https://doi.org/10.1144/SP538-2023-89, 2024.

Pfeifer, L. S., Wu, Q., Cui, Y., and Soreghan, G. S.: Modeling the impact of explosive volcanism on biogeochemical cycling at the peak of the Late Paleozoic icehouse, Glob. Planet. Change, 250, 104801, https://doi.org/10.1016/j.gloplacha.2025.104801, 2025.

Prospero, J. M., Ginoux, P., Torres, O., Nicholson, S. E., and Gill, T. E.: Environmental characterization of global sources of atmospheric soil dust identified with the Nimbus 7 Total Ozone Mapping Spectrometer (TOMS) absorbing aerosol product, Rev. Geophys., 40, 1002, https://doi.org/10.1029/2000RG000095, 2002.

Ruppert, L. F., Stanton, R. W., Cecil, C. B., Eble, C. F., and Dulong, F. T.: Effects of detrital influx in the Pennsylvanian Upper Freeport peat swamp, Int. J. Coal Geol., 17, 95–116, https://doi.org/10.1016/0166-5162(91)90006-5, 1991.

Sardar Abadi, M., Soreghan, G. S., Hinnov, L. A., Heavens, N. G., and Gleason, J. D.: Atmospheric dust flux in northeastern Gondwana during the peak of the Late Paleozoic Ice Age, Geol. Soc. Am. Bull., 133, 992–1006, https://doi.org/10.1130/B35636.1, 2021.

Scotese, C. R.: Tutorial: PALEOMAP PaleoAtlas for GPlates and the PaleoData Plotter Program, Technical Report 56, PALEOMAP Project, https://www.earthbyte.org/paleomap-paleoatlas-for-gplates/ (last access: 25 October 2026), 2016.

Scotese, C. R. and Wright, N. M.: PALEOMAP Paleodigital Elevation Models (PaleoDEMS) for the Phanerozoic, version v2, Zenodo [data set], https://doi.org/10.5281/zenodo.5460860, 2018.

https://doi.org/10.5194/egusphere-2026-6582
Preprint. Discussion started: 9 November 2026
© Author(s) 2026. CC BY 4.0 License.

Shao, Y., Wyrwoll, K.-H., Chappell, A., Huang, J., Lin, Z., McTainsh, G. H., Mikami, M., Tanaka, T. Y., Wang, X., and Yoon, S.: Dust cycle: An emerging core theme in Earth system science, Aeolian Res., 2, 181–204, https://doi.org/10.1016/j.aeolia.2011.02.001, 2011.

Shotyk, W.: Review of the inorganic geochemistry of peats and peatland waters, Earth-Sci. Rev., 25, 95–176, https://doi.org/10.1016/0012-8252(88)90067-0, 1988.

Shotyk, W.: Peat bog archives of atmospheric metal deposition: Geochemical evaluation of peat profiles, natural variations in metal concentrations, and metal enrichment factors, Environ. Rev., 4, 149–183, https://doi.org/10.1139/a96-010, 1996.

Spears, D. A. and Caswell, S. A.: Mineral matter in coals: Cleat minerals and their origin in some coals from the English Midlands, Int. J. Coal Geol., 6, 107–125, https://doi.org/10.1016/0166-5162(86)90015-7, 1986.

State Bureau of Petroleum and Chemical Industry: Analysis and identification of spore-pollen, SY/T 5915-2000 (in Chinese), https://std.samr.gov.cn/hb/search/stdHBDetailedCNF?id=8B1827F177FABB19E05397BE0A0AB44A (last access: 25 October 2026), 2000.

Susilawati, R. and Ward, C. R.: Metamorphism of mineral matter in coal from the Bukit Asam deposit, south Sumatra, Indonesia, Int. J. Coal Geol., 68, 171–195, https://doi.org/10.1016/j.coal.2006.02.003, 2006.

Tagliabue, A., Bowie, A. R., Boyd, P. W., Buck, K. N., Johnson, K. S., and Saito, M. A.: The integral role of iron in ocean biogeochemistry, Nature, 543, 51–59, https://doi.org/10.1038/nature21058, 2017.

Triplehorn, D. M.: Applications of tonsteins to coal geology: Some examples from western United States, Int. J. Coal Geol., 16, 157–160, https://doi.org/10.1016/0166-5162(90)90026-U, 1990.

Vertenstein, M., Bertini, A., Craig, T., Edwards, J., Levy, M., Mai, A., and Schollenberger, J.: CESM User's Guide (CESM1.2 Release Series User's Guide), NCAR Technical Note, CESM Software Engineering Group, National Center for Atmospheric Research, Boulder, CO, https://docs.cesm.ucar.edu/models/cesm1/user-guide/1.2/book1.html (last access: 13 October 2026), 2013.

Wang, F., Luo, M., He, Z., Ge, R., Cao, Y., De Grave, J., and Zhu, W.: Late Mesozoic intracontinental deformation and magmatism in the Chinese Tianshan and adjacent areas, Central Asia, Geol. Soc. Am. Bull., 134, 3003–3021, https://doi.org/10.1130/B36318.1, 2022.

Wang, H., Shao, L., Large, D. J., and Wignall, P. B.: Constraints on carbon accumulation rate and net primary production in the Lopingian (Late Permian) tropical peatland in SW China, Palaeogeogr. Palaeoclimatol. Palaeoecol., 300, 152–157, https://doi.org/10.1016/j.palaeo.2010.12.019, 2011.

Wang, H., Zeng, M., Peng, H., Zhu, C., Li, Y., Bai, Y., Zeng, Q., and Sun, J.: Significance of climate conditions in the variability of eolian dust deposition since the last deglaciation in the Zoigê region recorded by the Hongyuan peat, Quat. Sci., 43, 57–73, (in Chinese with English abstract), https://doi.org/10.11928/j.issn.1001-7410.2023.01.05, 2023.

Wang, L., Lv, D., Hower, J. C., Zhang, Z., Raji, M., Tang, J., Liu, Y., and Gao, J.: Geochemical characteristics and paleoclimate implication of Middle Jurassic coal in the Ordos Basin, China, Ore Geol. Rev., 144, 104848, https://doi.org/10.1016/j.oregeorev.2022.104848, 2022.

https://doi.org/10.5194/egusphere-2026-6582
Preprint. Discussion started: 9 November 2026
© Author(s) 2026. CC BY 4.0 License.

Wang, Y., Wang, W., Wang, W., and Duan, P.: Geochemical characteristics and sedimentary paleoenvironment of the coal-bearing strata in the Xishanyao Formation: A case study of the Yihua Coal Mine in the Zhundong Coalfield, Xinjiang, Minerals, 14, 461, https://doi.org/10.3390/min14050461, 2024.

Ward, C. R.: Analysis, origin and significance of mineral matter in coal: An updated review, Int. J. Coal Geol., 165, 1–27, https://doi.org/10.1016/j.coal.2016.07.014, 2016.

Weedon, G. P.: Time-Series Analysis and Cyclostratigraphy: Examining Stratigraphic Records of Environmental Cycles, Cambridge University Press, Cambridge, https://doi.org/10.1017/CBO9780511535482, 2003.

Zhang, Z., Wang, C., Lv, D., Hay, W. W., Wang, T., and Cao, S.: Precession-scale climate forcing of peatland wildfires during the early middle Jurassic greenhouse period, Glob. Planet. Change, 184, 103051, https://doi.org/10.1016/j.gloplacha.2019.103051, 2020.

Zhang, Z., Wang, T., Ramezani, J., Lv, D., and Wang, C.: Climate forcing of terrestrial carbon sink during the Middle Jurassic greenhouse climate: Chronostratigraphic analysis of the Yan'an Formation, Ordos Basin, North China, Geol. Soc. Am. Bull., 133, 1723–1733, https://doi.org/10.1130/B35765.1, 2021.

Zhang, Z., Lv, D., Lu, M., Yu, Z., Gao, Y., Wang, T., Gao, J., and Wang, C.: Wildfire activity driven by the 405-kyr orbital climate cycles in the Middle Jurassic, Glob. Planet. Change, 222, 104069, https://doi.org/10.1016/j.gloplacha.2023.104069, 2023.

Zhong, Y., Liu, Y., Yang, H., Yin, Q., Wilson, D. J., Lu, Z., Jaccard, S. L., Struve, T., Clift, P. D., Kaboth-Bahr, S., Larrasoaña, J. C., Bahr, A., Gong, X., Zhao, D., Zhang, Y., Xia, W., and Liu, Q.: Orbital controls on North Pacific dust flux during the late Quaternary, Geophys. Res. Lett., 51, e2023GL106631, https://doi.org/10.1029/2023GL106631, 2024.